Electronic Supplementary Material (ESI) for Faraday Discussions.

Electronic Supplementary Information (ESI)

A unified view on heterogeneous and homogeneous catalysts through a combination of spectroscopy and quantum chemistry

Dimitrios Maganas, Annette Trunschke, Robert Schlögl and Frank Neese**

Table of Contents

Chemical Importance of the homogeneous and heterogeneous examples

As an example of a homogeneous catalyst we present in this work the K[VO(O_2)Hheida] oxo-peroxo vanadium complex. In general vanadium oxo-peroxo complexes contain the vanadyl oxygen and peroxo functional groups, which are considered possible candidates to form oxygenated products in oxidation reactions.[1-4] The molecular structure of K[VO(O_2)Hheida] together with the active catalytic ionic form [VO(O_2)Hheida]$^-$ is visualized in Figure 1 (top and bottom-left). Furthermore, the possible presence of the oxygen deficient Hheida ion [VO(O)Hheida]$^-$ is considered when an oxygen atom, is removed from the peroxo group of [VO(O_2)Hheida]$^-$ (Figure 1, bottom-right).

The complementary example from heterogeneous catalysis refers to silica supported vanadia catalysts. Mono- and submono-layer-type silica-supported vanadia oxide catalysts, $VO_{x/}SiO_{2,}$ depict manifold structural facets of surface vanadium oxide species. Their molecular structure can be adjusted to some degree by vanadia loading and preparation technique.[5] Silica-supported vanadium oxides have therefore been considered as models for vanadium oxide based catalysts[6-11] However, despite extensive research, there are still fundamental aspects of these metal-oxide catalysts that are not well understood. In particular, the nature of the active vanadium species that is involved in the elementary catalytic steps of the above mentioned reactions are still controversially debated, especially in the case of the silica-supported catalysts.[12, 13] Among various classes of materials to support the active VO_x species, mesoporous silica SBA-15 provides an attractive choice to systematically design a monolayer type of highly dispersed vanadia-based catalytic centers.[11, 14] In practice, three possibilities for the vanadium oxide-supported structures exist, which range from monomeric species, to oligomers ending up to crystalline V_2O_5 if the monolayer coverage is exceeded.[15-17] The question, whether the degree of oligomerization matters, remains unclear due to the complexity of the spectroscopic patterns featured by supported vanadium oxide and the challenges originating from synthesis. The present work represents a dedicated effort to address this question through an analysis of the spectroscopic data in conjunction with quantum chemical calculations.

Experimental procedures

Synthesis

The synthesis of VOx/SBA-15 catalyst has been presented in detail elsewhere[10]
The synthesis of the molecular complex was described in dx.doi.org/10.1021/jp5081719 | J. Phys. Chem. C 2014, 118, 24611−24622.

UV/Vis spectroscopy[10]

UV-Vis spectra were measured with a Perkin-Elmer Lambda 650 instrument using a diffuse reflectance accessory (Harrick PrayingMantis) complete with environmental chamber attachment (HarrickHVC-VUV-4). To avoid saturation on strongly absorbing signals samples were diluted 20-fold with calcined bare SBA-15 from the same batch used to prepare the catalyst. Spectra were recorded at room temperature after the mixtures were dehydrated in synthetic air (20% O2, 80% Ar, total flow of 60 ml min^{-1}) at 723 K for a period of 60 min. Dehydrated SBA-15 was used as a white reference. Tungsten–halogen and deuterium lamps were used as light sources allowing spectra to be recorded in the range 200–800 nm. Reflectance data were converted to Kubelka–Munk units.

Raman spectroscopy[10]

Raman spectra of the silica-supported vanadia catalysts were recorded by using a triple filter Raman spectrometer (TriVista S&I GmbH) with a CCD camera (Princeton Instruments) as the detector attached to a confocal microscope (Olympus, 10" long-working distance objective), using an Ar+ laser with 488 nm excitation wavelength (1 mW on the sample). The spectrometer was operated in triple subtractive mode and each spectrum was integrated for 2–10 min as required to produce spectra with an acceptable signal to noise ratio. A two-point wavelength calibration was used (laser wavelength and first-order Stokes phonon of Si at 520 cm^{-1}).

Raman spectroscopy of the molecular complex was performed using a confocal Raman microscope system, TriVista TR557 (S&I GmbH), equipped with an Olympus BX51 microscope (10× objective), a 532 nm DPSS Laser (excitation at ~0.7 mW), and a Princeton Instruments SP-2750i monochromator

(750 mm focal length) with a N_2-cooled CCD. The measurement was optimized in terms of exposure time and laser intensity to avoid decomposition of the sample.

X-Ray spectroscopy

In situ NEXAFS measurements were performed at the synchrotron radiation facility BESSY in Berlin (Germany) using the ISISS (Innovative Station for In Situ Spectroscopy) beamline as a tuneable X-ray source. High-pressure soft X-ray absorption was measured in the presence of oxygen using the high pressure station designed and constructed at the Fritz Haber Institute, Berlin. Details of the setup are described elsewhere.[18] The catalyst powders have been pressed into self-supporting discs (1t, 8 mm diameter) and mounted inside a cell onto a sapphire sample holder approximately 1.4mmin front of the first aperture of a differentially pumped electrostatic lens system. The home-built electron lens serves as the input system for amodified commercial hemispherical electron analyzer (PHOIBOS 150, Specs GmbH). Oxygen is introduced into the cell via a calibrated mass flow controller, heating is provided by a NIR laser at the rear of the sample, and the temperature is monitored by a thermocouple attached directly to the sample surface. NEXAFS spectra of the dehydrated samples were obtained in 50 Pa O_2 at 673 K by heating the material in-situ in the XAS cell with 5 K min^{-1} up to the final temperature. Oxygen K-edge excitation spectra have been recorded in the Auger electron yield mode by operating the electron spectrometer with a pass energy of 100 eV as an X-ray absorption spectroscopy (XAS) detector to minimize contributions from the gas phase to the spectra. O K-edge spectra of the sample surface have been corrected for the remaining effects of O_2 gas phase absorption. In order to increase the signal to noise ratio a data reduction by a factor 2 has been applied to the raw spectra (containing about 1000 pts per scan) by averaging adjacent points. Three scans have been averaged and the X-ray spot position on the sample has been changed after each scan to avoid damage of the surface by the brilliant synchrotron X-ray beam. Absolute energy calibration has been achieved by setting the π^* resonance of the O_2 gas phase signal to 530.9 eV and the spectral resolution was about 150 meV. Further details of the methodology and data treatment are described elsewhere.[19]

Description of the parameterization procedure

The composition of the contributing Si/V centers to the low loading experimental V L-edge spectra was estimated via a parameterization procedure. At first spectra combinations were generated containing contributions from monomeric, dimeric, trimeric and tetrameric model clusters. These spectra were then fitted to the experimental 2%V loading V L-edge L_3 spectrum. Such procedure involves a constrained multi-gaussian least square fitting by employing the Lavenberg-Marquardt algorithm. The chosen gaussians have the general form:

$$f(x) = Amp \times \frac{1}{\sqrt{2\pi \times FWHM^2}} e^{-\frac{(x-Centroid)^2}{2\times FWHM}}$$

Where Amp is the amplitude, FWHM is the full width at half maximum and Centroid is the position of the defined Gaussian. Tight convergence criteria are used for the relative error in the approximate solution ($x_{tol}=10^{-8}$) as well as for the desired sum of squares ($f_{tol}=10^{-8}$). The quality of the fit is measured with the aid of the following parameters: First,

$$SS_{err} = \chi^2 = \sum_{i}^{gridpoints} \left(y_i^{exp} - y_i^{model}(\nu)\right)^2$$

where SS_{err}, is the regression sum of the squares which is the sum of the squares of the deviations of the predicted values y_i^{model} from the experimental values y_i^{exp}. Second,

$$SS_{tot} = \sum_{i}^{gridpoints} \left(y_i^{model} - \bar{y}(\nu)\right)^2$$

where SS_{tot} is the total sum of the squares of the deviation of the predicted values y_i^{model} from the average experimental value $\bar{y}_i^{model}$ and eventually

$$R^2 = 1 - \frac{SS_{err}}{SS_{tot}}$$

where R^2 is usually referred to as the coefficient of determination. It provides a measure for the goodness of fit and takes values between 0 and 1. In this work R^2 is used as a normalized version of SS_{err} and refers here as an indicator of the quality of the fitting throughout the parameterization procedure.

Computational details

All calculations were performed with the ORCA suite of programs.[20] The BP86[21, 22] and B3LYP[21, 23, 24] functionals were used together with Grimme's dispersion correction[25, 26] for geometries/frequencies and electronic properties, respectively. The def2−TZVP basis set of Wigend et al.[27] is of triple-ζ quality[28] and was used for all the atoms in combination with the matching Coulomb fitting basis for the resolution of identity[29, 30] (RI, in BP86 calculations). Scalar relativistic effects were treated on the basis of the second−order Douglas−Kroll−Hess (DKH).[31-33] The vibrational frequenies were calculated at the B3LYP level since it has shown excellent agreement between calculated frequensies and observef fundamental vibrational peaks. The optical spectra were caclulated by time depended density functional theory (TD-DFT) for the first 100 non-relativistic roors. Excited-state displacements relative to the ground state equilibrium geometry were calculated according to the relation:

$$\Delta_{Q,k} = \Delta_{Q,k_0} - \Delta_{Q,g_0}$$

where Δ_{Q,k_0} and Δ_{Q,g_0} are the shifts along the *k*th normal mode of the excited- and ground state-minima relative to the ground state equilibrium geometry. Using the information of the above frequencies and excited states calculations the absorption band shape as well as the Raman profile intensities arising from the lowest calculated excited states were evaluated by the orca_asa module.[34-37] Vanadium L-edge and oxygen K-edge spectra were calculated via the DFT/ROCIS protocol. These calculations were performed using the converged restricted RKS Kohn−Sham wavefunctions. For these calculations, the B3LYP density functionals was employed together with the def2-SVP and def2−TZVP(-f) basis sets. In a typical calculation 40-80 roots were calculated to ensure saturation of involved excitations. The absorption spectra were obtained from DFT/ROCIS calculated intensities by applying a Gaussian broadening of 0.8 eV to the calculated transitions for both V L-edge and O K-edge spectra. It should be noted that in these calculations the spin-orbit splitting (SOC) is underestimated by about 3-4%.[38, 39] In addition, the intensity of the main L_2 signal is usually underestimated as the energy position and/or the intensities of the L_2 region are subject to distortions and broadening due to the Coster-Kronig Auger decay,[40] which cannot be estimated in the calculations.[38]

Electronic Structure (An Example)

In a first approximation it is convenient to analyse the electronic structure of these systems and explore the anisotropic coordination environment of the V-O bonding on the basis of 1-electron particle/hole approach by relying on basic expectations from Ligand Field theory. This is best done for the well defined structure of the molecular catalyst $[VO(O_2)Hheida]^-$. In fact, the covalent nature involving σ and

π interactions between the vanadium center and the oxo, peroxo and ligand oxygen atoms is presented at Figure 7. Under approximately C_{3v} symmetry both complexes have $^1A_1$ ground states with $1e^2 1a_1^2 2e^0 3e^0 2a_1^0$ electron configurations consistent with the V^{5+} oxidation state (Figures 7, S3). Within the 1-electron particle/hole excitation scheme the key ligand field excited states are of Ligand to Metal Charge Transfer (LMCT) nature involving electron excitations from the $p_{x,y,z}$ oxo, peroxo and ligand oxygen orbitals. As can be seen in Figure 7 and Figure S3 for both complexes these excitations can be grouped in two main categories depending on the nature of the donor orbital. For the $[VO(O_2)Hheida]^-$ complex the first involves excitations from the $2p_z^{Peroxo}$orbitals that result to states involving two π, $^1\mathrm{E}(1a_1 \rightarrow 2e)$, $^1\mathrm{E}(1a_1 \rightarrow 3e)$ and one σ, $^1A_1(1a_1 \rightarrow 2a_1)$ interaction, respectively. In addition, the second category involves excitations from the 2p orbital of both oxo, peroxo and ligand oxygen atoms giving rise to states with σ and π interactions:

$^1A_1 + ^1A_2 + ^1E(1e \rightarrow 2e)$, $^1A_1 + ^1A_2 + ^1E(1e \rightarrow 3e)$ and $^1E(1e \rightarrow 2a_1)$. Similar arguments can be drawn for the $[VO(O)Hheida]^-$ complex. By inspecting Figure S3 however, significant changes are expected due to the fact that the oxo-peroxo ($V\text{-}OO_2$) functionality has been transformed to a bis-oxo (V-OO) one. These differences are explored in detail in the main text. We should highlight however that the observed experimental spectroscopic features can only be explored through direct calculation of the corresponding many particle spectra. Hence, the analysis presented above is only valid for qualitative purposes.

Figures

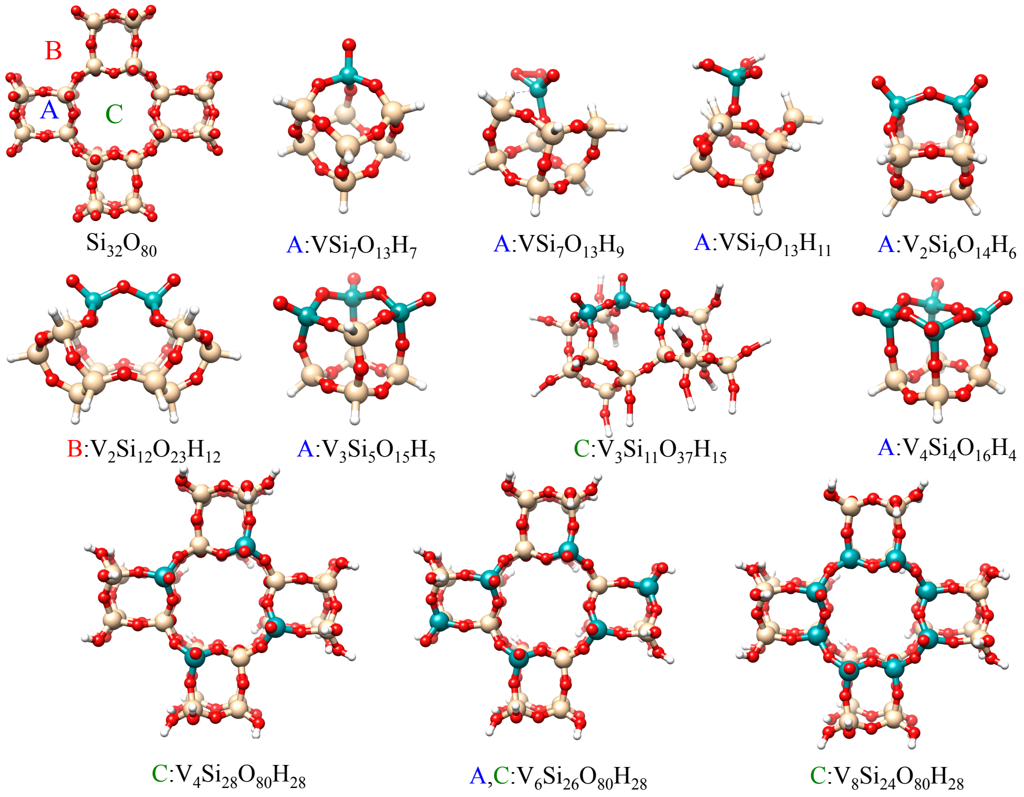

Figure S1.
Graphical representation of the cluster models used to model the different silica supported vanadia centers. The models were constructed from a bilayer silica fragment ($Si_{32}O_{80}$) extracted from the crystallographic structure of SiO_2.[41] Letters A, B and C indicate the different domains of the $Si_{32}O_{80}$ fragment that were used to construct the models. Cyan, pale-yellow, red and white indicate vanadium, silica oxygen and hydrogen atoms, respectively.

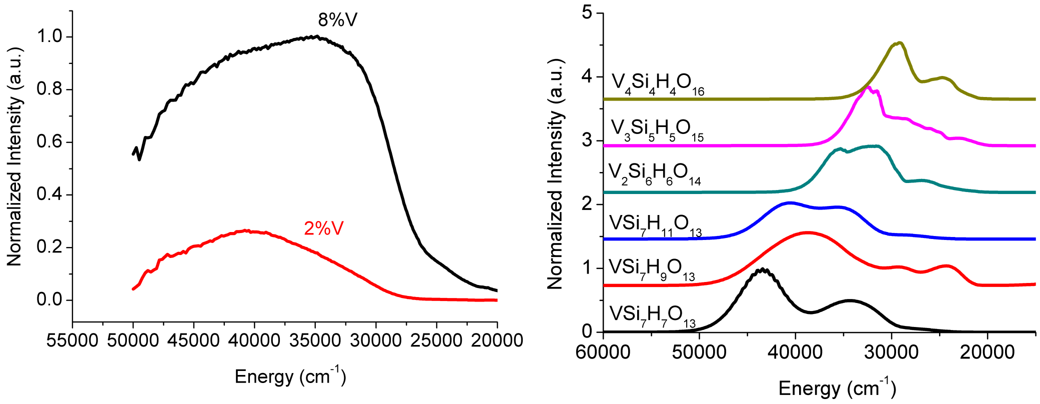

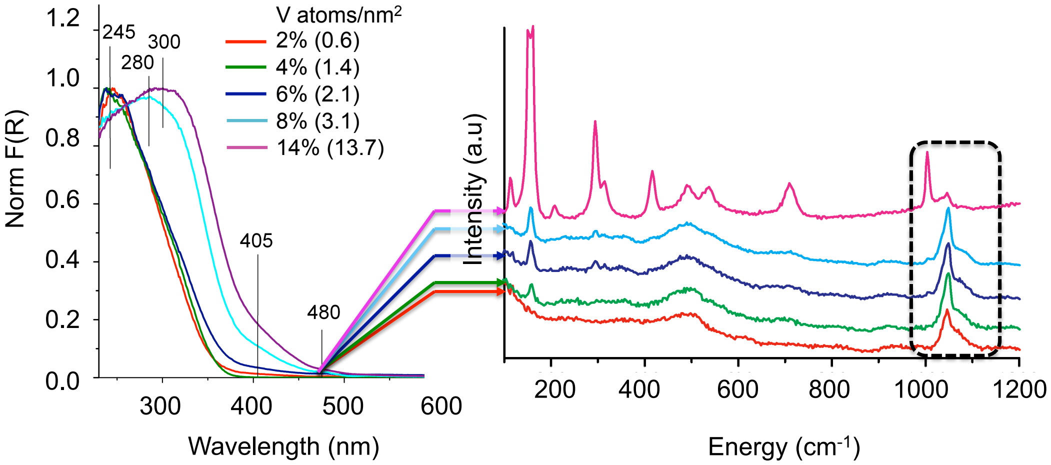

Figure S2.

Top-Left: experimental UV/Vis spectra for two vanadium loadings (2 and 8%). Top-Right: calculated B3LYP/TD-DFT absorption spectra for selected models with increasing vanadium centers. In agreement with the experiment shown also in Fig.2, the spectra shift at lower energies as the vanadium loading increases. Bottom: UV/Vis and Raman spectra (measured upon excitation by a 488 nm laser) of dehydrated V/SBA-15 for sever vanadium loadings. The dashed black window highlights the Raman signal located at 1000-1100 cm^{-1}.

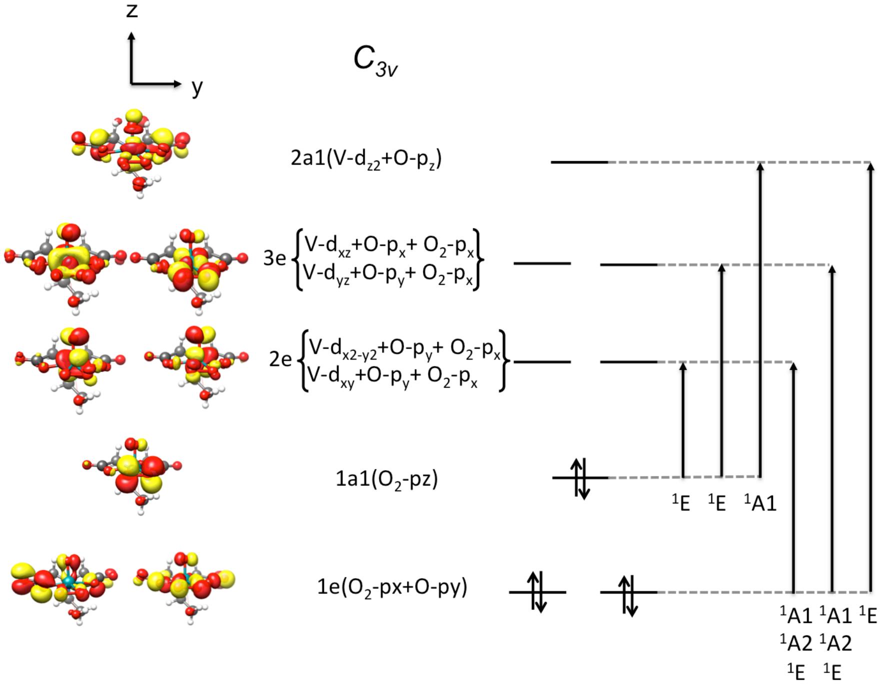

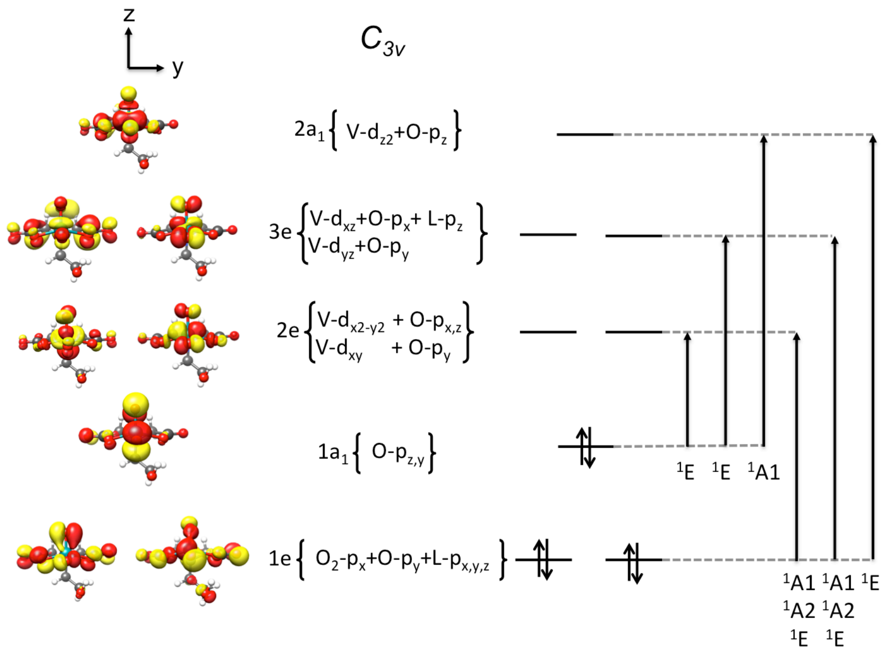

Figure S3.

The MO splitting diagram of the local V-OO_2 (*C_{3v}*) core (top) and V-OO (*C_{3v}*) core (bottom). In addition, the adapted 2p-3d transitions in the one electron particle/hole approximation are visualized assuming ideal *C_{3v}* ligand fiield splittings.

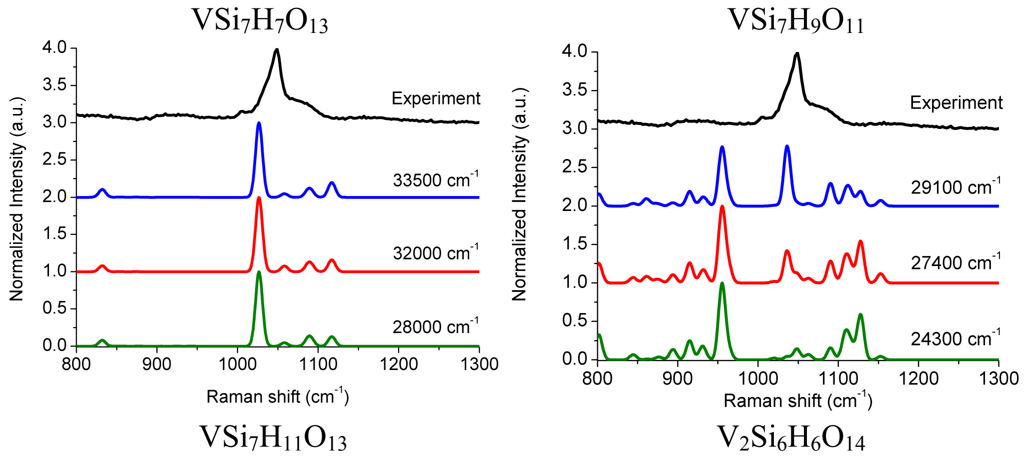

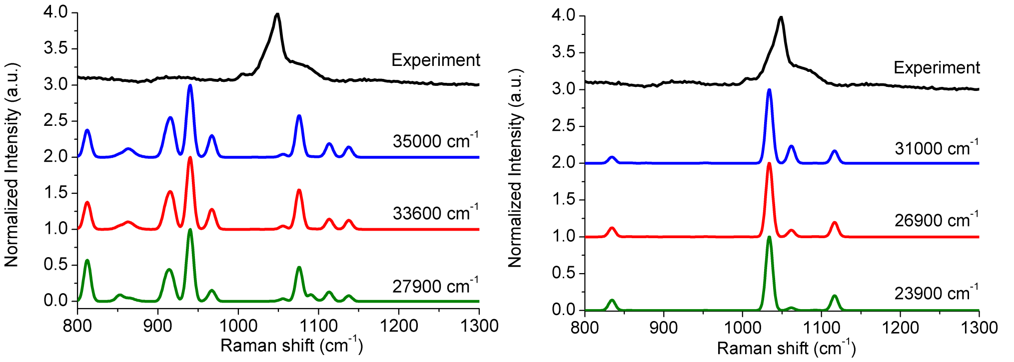

$V_3Si_5H_5O_{15}$ $V_4Si_4H_4O_{16}$

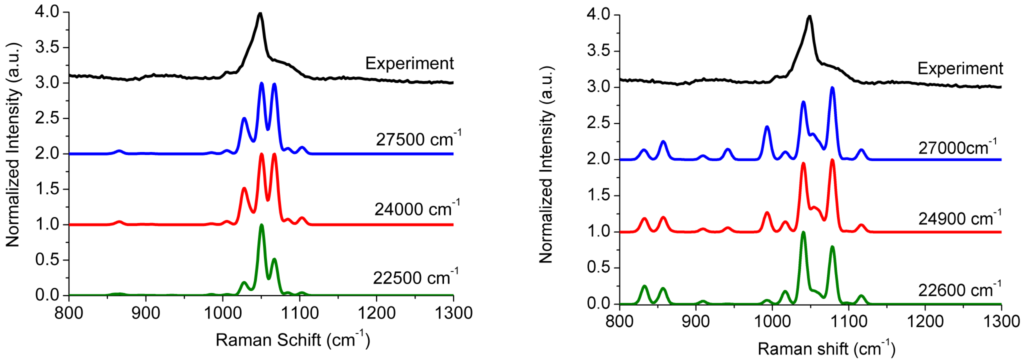

Figure S4.
For the model complexes belonging on the A-domain as is shown in Fig.S2 the corresponding resonance Raman spectra are evaluated at three energy positions of the corresponding absorption spectra (Fig.S3). The experimental spectrum corresponds to 2 % V loading.

$V_2Si_{12}H_{12}O_{23}$

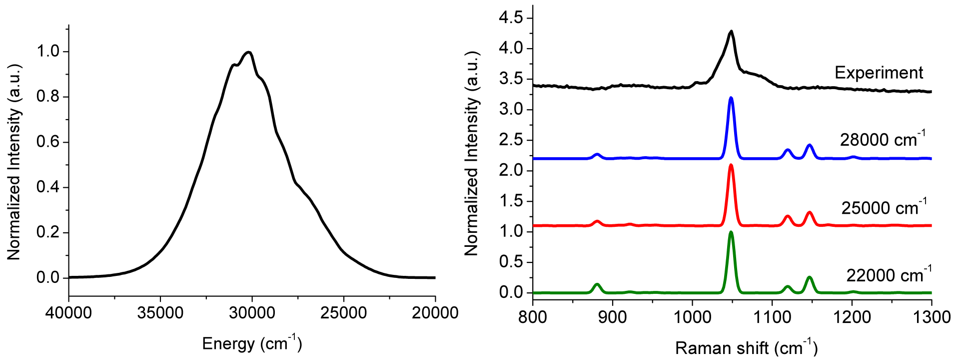

$V_3Si_{11}H_{15}O_{37}$

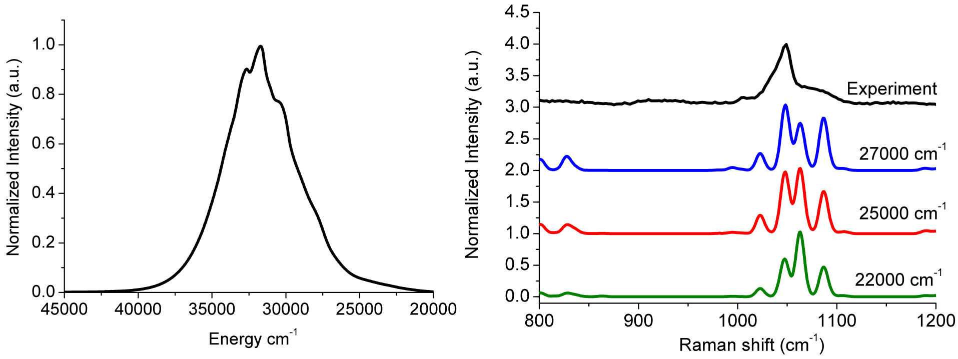

$V_4Si_{28}H_{28}O_{80}$

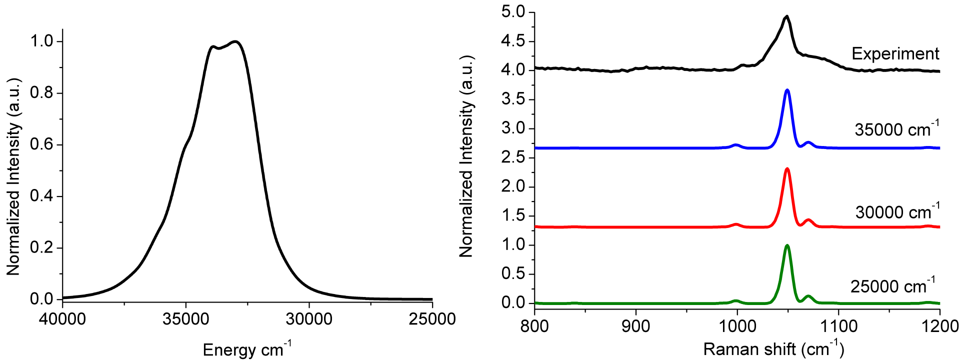

Figure S5.

Three representative model complexes originating from B and/or C-domains shown in Fig.S1 (namely $V_2Si_{12}H_{12}O_{23}$, $V_3Si_{11}H_{15}O_{37}$ and $V_4Si_{28}H_{28}O_{80}$) for which the resonance Raman spectra were evaluated at three energy positions of the corresponding absorption spectra shown on the left side. The experimental spectrum corresponds to 2 % V loading.

$VSi_7H_7O_{13}$ $VSi_7H_9O_{11}$

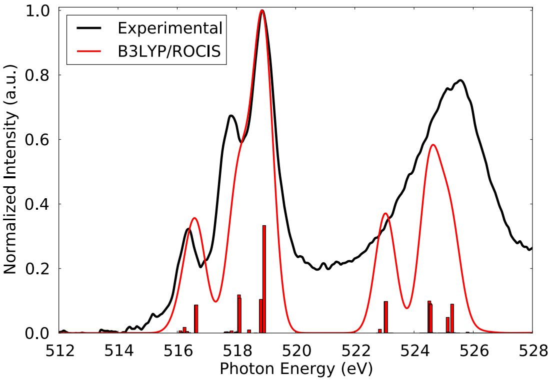

$VSi_7H_{11}O_{13}$

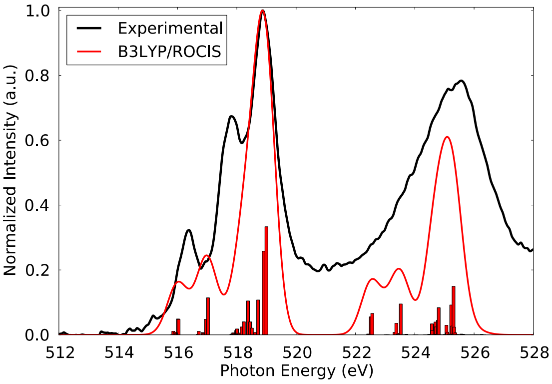

$V_2Si_6H_6O_{14}$

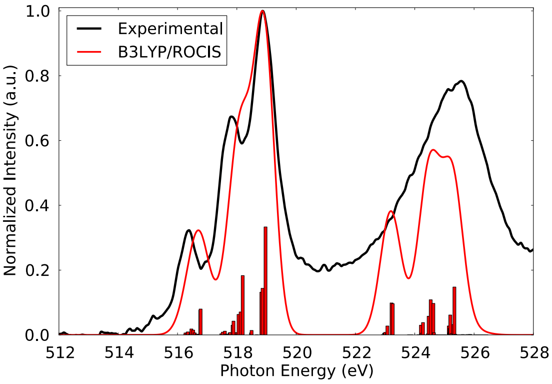

$V_3Si_5H_5O_{15}$

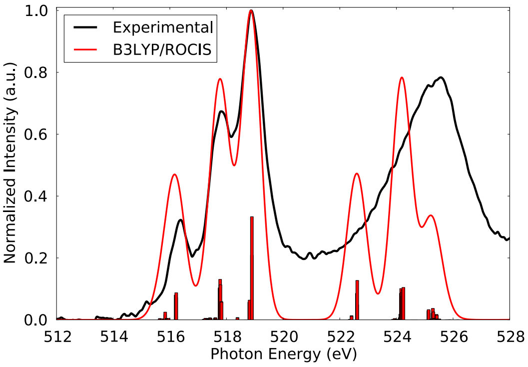

$V_4Si_4H_4O_{16}$

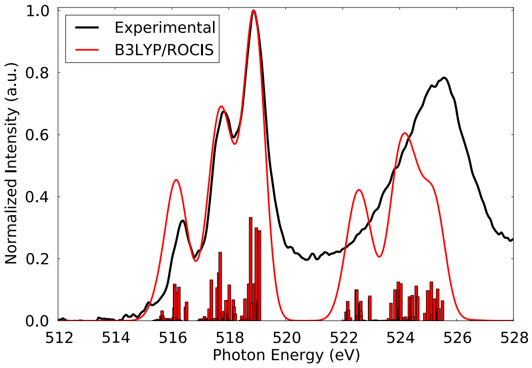

$V_2Si_{12}H_{12}O_{23}$

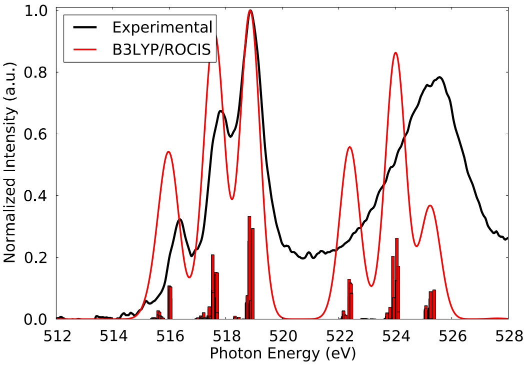

$V_3Si_{11}H_{15}O_{37}$

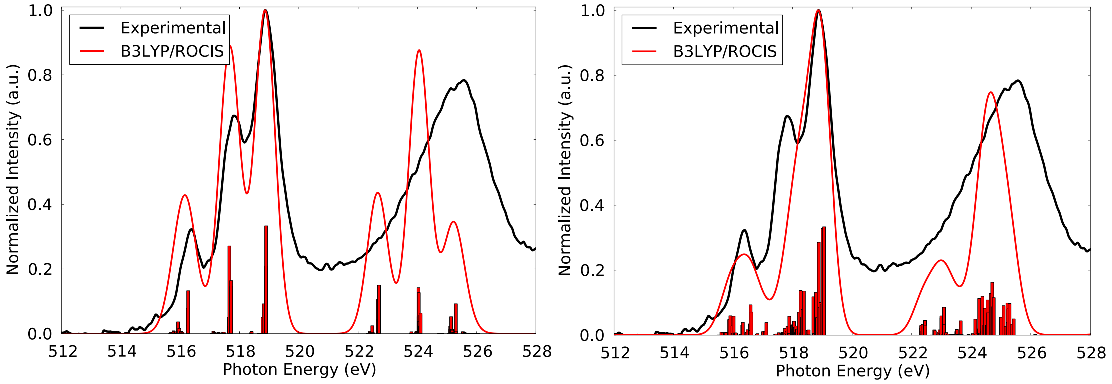

$V_4Si_{28}H_{28}O_{80}$ $V_6Si_{26}H_{28}O_{80}$

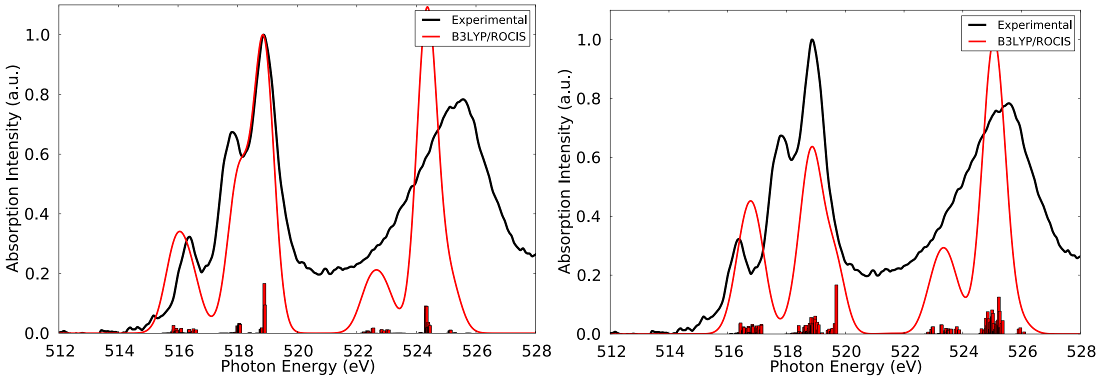

$V_8Si_{24}H_{28}O_{80}$

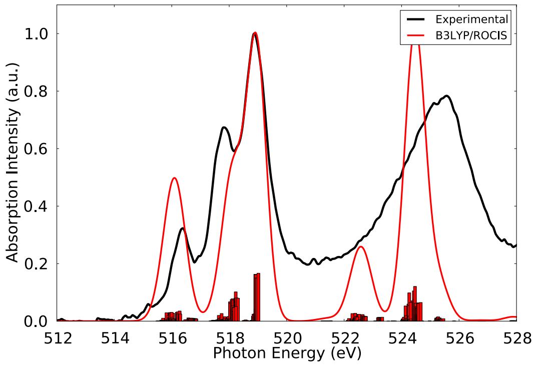

Figure S6.

Experimental (black) versus calculated (red) V L-edge spectra for the model complexes originating form the A, B and C-domains as is shown in Fig.S1. Red sticks indicate calculated relativistic states. The experimental spectrum corresponds to 2 % V loading.

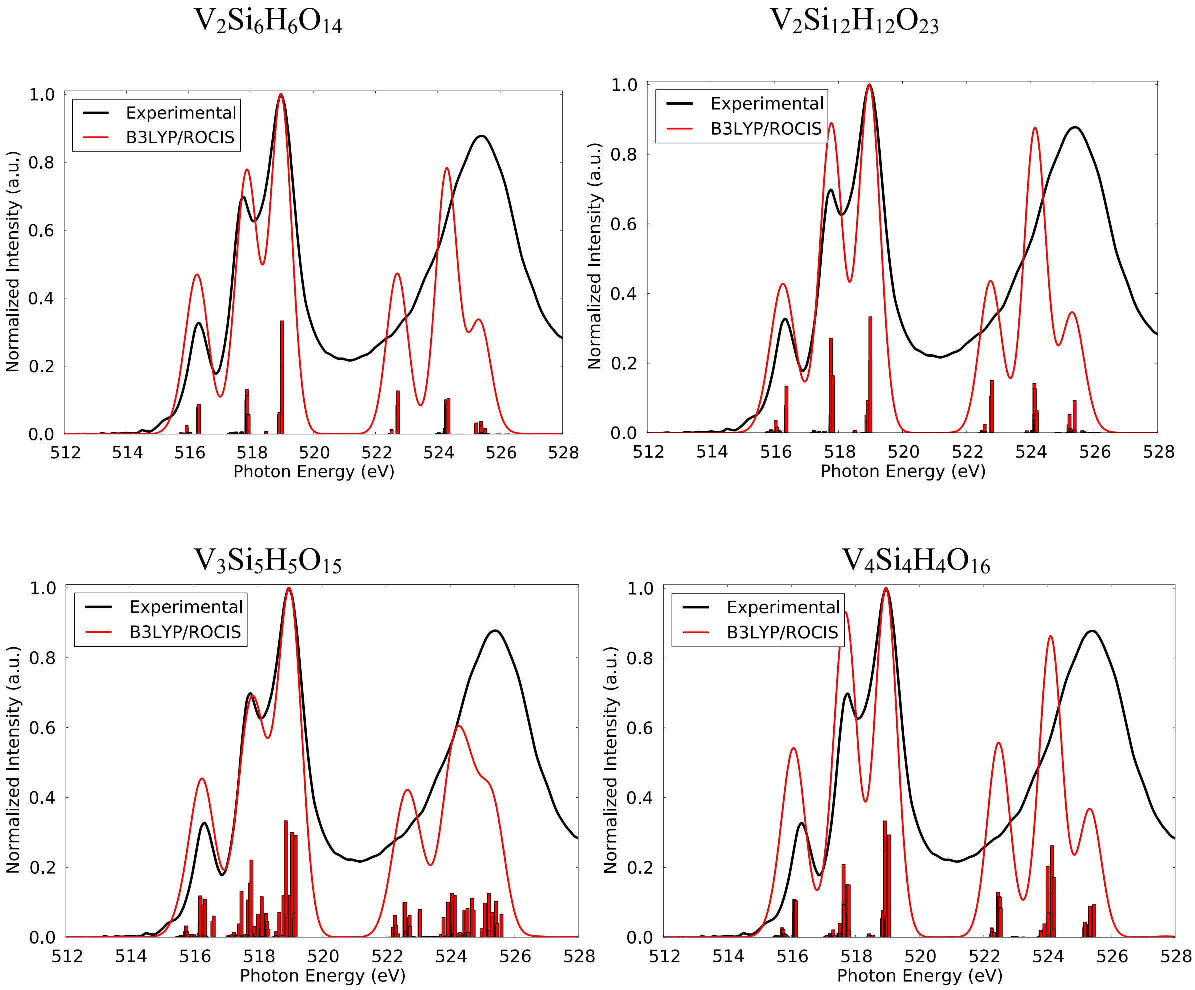

Figure S7.

Experimental (black) versus calculated (red) V L-edge spectra for the model complexes $V_2Si_6H_6O_{14}$, $V_2Si_{12}H_{12}O_{23}$, $V_3Si_5H_5O_{15}$ $V_4Si_4H_4O_{16}$ Red sticks indicate calculated relativistic states. The experimental spectrum corresponds to 8 % V loading.

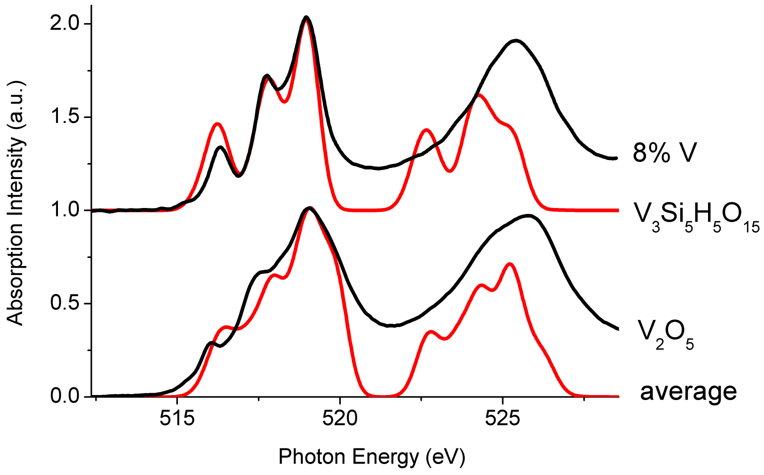

Figure S8.
Comparison between the experimental black: 8 %V and V_2O_5 spectra with the DFT/ROCIS calculated red: $V_3Si_5H_5O_{15}$ and the average spectrum resulted from summation of the $V_2Si_6H_6O_{14}$, $V_2Si_{12}H_{12}O_{23}$, $V_3Si_5H_5O_{15}$ and $V_4Si_4H_4O_{16}$ individual spectra. An offset is introduced to highlight the close resemblance between groups of calculated and experimental spectra.

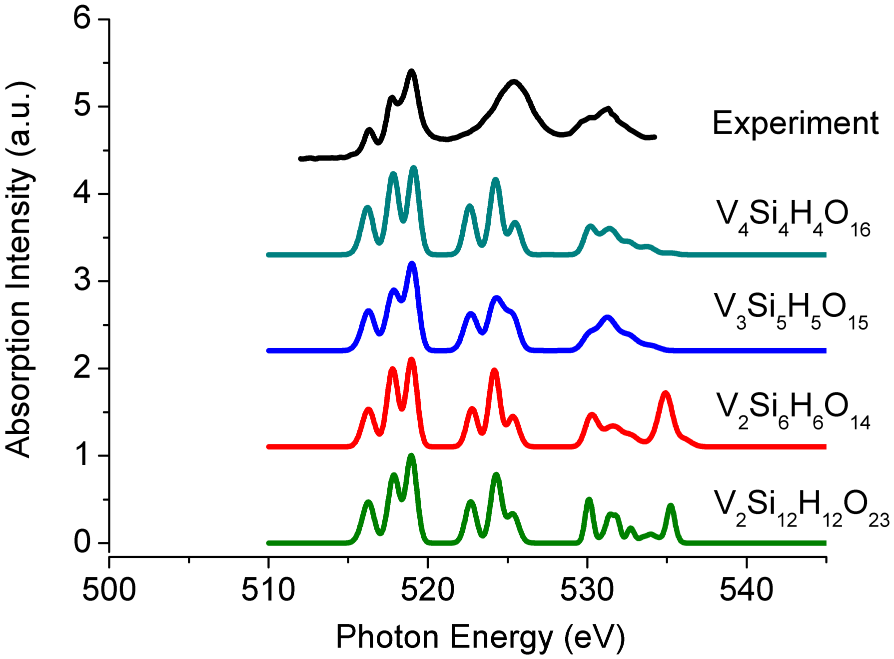

Figure S9.
For the structures that have shown good agreement between theory and experiment for Raman and V L-edge spectroscopy ($V_2Si_6H_6O_{14}$, $V_2Si_{12}H_{12}O_{23}$, $V_3Si_5H_5O_{15}$ and $V_4Si_4H_4O_{16}$), in a further step of analysis the corresponding O K-edge spectra are compared. The experimental spectrum corresponds to 2 % V loading.

Tables

Table S1

Selected experimental and calculated V-O bond distances and bond orders for [VO(O_2)Hheida]$^-$ and [VO(O)Hheida]$^-$ complexes

		Experiment	Calculations	
	Functional group	Bond Distances(Å)	Bond Distances(Å)	Löwdin Bond Order
[VO(O_2)Hheida]$^-$	V=O	1.60	1.60	2.66
	V-O_2	1.84	1.85	1.26
[VO(O)Hheida]$^-$	V=O	-	1.62	2.61
	V=O	-	1.62	2.61

Bibliography

1. M. Casny and D. Rehder, *Chemical Communications*, 2001, 921-922.
2. M. Casny and D. Rehder, *Dalton Transactions*, 2004, 839-846.
3. G. J. Colpas, B. J. Hamstra, J. W. Kampf and V. L. Pecoraro, *Journal of the American Chemical Society*, 1996, **118**, 3469-3478.
4. O. L. J. Gijzeman, J. N. J. van Lingen, J. H. van Lenthe, S. J. Tinnemans, D. E. Keller and B. M. Weckhuysen, *Chemical Physics Letters*, 2004, **397**, 277-281.
5. B. M. Weckhuysen and D. E. Keller, *Catalysis Today*, 2003, **78**, 25-46.
6. J. L. Nieto, *Top Catal*, 2006, **41**, 3-15.
7. B. Grzybowska-Świerkosz, *Applied Catalysis A: General*, 1997, **157**, 263-310.
8. P. Forzatti, *Appl. Catal., A*, 2001, **222**, 221.
9. E. A. Mamedov and V. Cortés Corberán, *Applied Catalysis A: General*, 1995, **127**, 1-40.
10. P. Gruene, T. Wolfram, K. Pelzer, R. Schlögl and A. Trunschke, *Catalysis Today*, 2010, **157**, 137-142.
11. N. Hamilton, T. Wolfram, G. T. Mueller, M. Haevecker, J. Kroehnert, C. Carrero, R. Schomaecker, A. Trunschke and R. Schlögl, *Catalysis Science & Technology*, 2012, **2**, 1346-1359.
12. J. E. Molinari and I. E. Wachs, *Journal of the American Chemical Society*, 2010, **132**, 12559-12561.
13. C. Hess, *ChemPhysChem*, 2009, **10**, 319-326.
14. C. Hess, U. Wild and R. Schlögl, *Microporous and Mesoporous Materials*, 2006, **95**, 339-349.
15. A. Khodakov, B. Olthof, A. T. Bell and E. Iglesia, *Journal of Catalysis*, 1999, **181**, 205-216.
16. I. E. Wachs, *Dalton Transactions*, 2013, **42**, 11762-11769.
17. M. D. Argyle, K. Chen, A. T. Bell and E. Iglesia, *Journal of Catalysis*, 2002, **208**, 139-149.
18. A. Knop‐Gericke, E. Kleimenov, M. Hävecker, R. Blume, D. Teschner, S. Zafeiratos, R. Schlögl, V. I. Bukhtiyarov, V. V. Kaichev, I. P. Prosvirin, A. I. Nizovskii, H. Bluhm, A. Barinov, P. Dudin and M. Kiskinova, in *Advances in Catalysis*, eds. C. G. Bruce and K. Helmut, Academic Press, 2009, vol. Volume 52, pp. 213-272.
19. M. Hävecker, M. Cavalleri, R. Herbert, R. Follath, A. Knop-Gericke, C. Hess, K. Hermann and R. Schlögl, *physica status solidi (b)*, 2009, **246**, 1459-1469.
20. F. Neese, *Wiley Interdisciplinary Reviews: Computational Molecular Science*, 2012, **2**, 73-78.
21. A. D. Becke, *Phys. Rev. A*, 1988, **38**, 3098-3100.
22. J. P. Perdew, *Phys. Rev. B*, 1986, **33**, 8822-8824.
23. A. D. Becke, *J. Chem. Phys.*, 1993, **98**, 5648.
24. C. Lee, W. Yang and R. G. Parr, *Phys. Rev. B*, 1988, **37**, 785.
25. S. Grimme, J. Antony, S. Ehrlich and H. Krieg, *J. Chem. Phys.*, 2010, **132**, 154104.
26. S. Grimme, S. Ehrlich and L. Goerigk, *Journal of Computational Chemistry*, 2011, **32**, 1456-1465.
27. F. Weigend and R. Ahlrichs, *Physical Chemistry Chemical Physics*, 2005, **7**, 3297-3305.
28. A. Schäfer, C. Huber and R. Ahlrichs, *J. Chem. Phys.*, 1994, **100**, 5829-5835.
29. M. Feyereisen, G. Fitzgerald and A. Komornicki, *Chem. Phys. Lett.*, 1993, **208**, 359.
30. R. A. Kendall and H. A. Früchtl, *Theor. Chem. Acc.*, 1997, **97**, 158.
31. B. A. Hess, *Phys.Rev. A*, 1985, **32**, 756.
32. B. A. Hess, *Phys.Rev. A*, 1986, **333**, 3742.
33. G. Jansen and B. A. Hess, *Phys.Rev. A*, 1989, **39**, 6016.

34. F. Neese, T. Petrenko, D. Ganyushin and G. Olbrich, *Coordination Chemistry Reviews*, 2007, **251**, 288-327.
35. T. Petrenko, S. Kossmann and F. Neese, *Journal of Chemical Physics*, 2011, **134**.
36. T. Petrenko and F. Neese, *Journal of Chemical Physics*, 2007, **127**.
37. T. Petrenko and F. Neese, *Journal of Chemical Physics*, 2012, **137**.
38. M. Roemelt, Maganas, D., DeBeer, S, Neese, F., *J. Chem. Phys.*, 2013, **138**, 204101.
39. D. Maganas, M. Roemelt, M. Havecker, A. Trunschke, A. Knop-Gericke, R. Schlögl and F. Neese, *Physical chemistry chemical physics : PCCP*, 2013, **15**, 7260-7276.
40. D. Coster and R. D. L. Kronig, *Physica*, 1935, **2**, 13-24.
41. P. Villars, K. Cenzual, J. Daams, R. Gladyshevskii, O. Shcherban, V. Dubenskyy, V. Kuprysyuk, I. Savysyuk and R. Zaremba, in *Structure Types. Part 10: Space Groups (140) I4/mcm – (136) P42/mnm*, eds. P. Villars and K. Cenzual, Springer Berlin Heidelberg, 2011, vol. 43A10, ch. 538, pp. 632-633.